PCCP
Physical Chemistry Chemical Physics

# Accepted Manuscript

This article can be cited before page numbers have been issued, to do this please use: B. Politov, S. García-Martín and I. R. Shein, *Phys. Chem. Chem. Phys.*, 2025, DOI: 10.1039/D5CP01780G.




ROYAL SOCIETY OF CHEMISTRY

rsc.li/pccp

# Highly anisotropic electronic properties of the $GdBa_2Ca_2Fe_5O_{13}$ oxide: a DFT+U study of a potential air electrode for solid oxide fuel cells

View Article Online
DOI: 10.1039/D5CP01780G

Politov Boris[1]*, Igor Shein[2] and Susana Garcia-Martin[1]*

[1] *Universidad Complutense de Madrid, 28040, Madrid, Spain*

[2] *Institute of Solid State Chemistry UB RAS, 620990, Yekaterinburg, Russia*

*corresponding emails: politoffboris@yandex.com and sgmartin@quim.ucm.es





## Abstract

Profound knowledge of the electronic structure of functional solids is essential to understand and optimize their properties. The current advances in electronic structure theory, together with the improvements in computing power, permit to realize affordable calculations of electronic structure of complex solids with the aim of explaining or predicting properties of singular materials. This work presents a Density Functional Theory study of the $GdBa_2Ca_2Fe_5O_{13}$ oxide, a potential air electrode for solid oxide fuel cells with layered-perovskite-related structure, which presents ordering of three different coordination-polyhedron around the $Fe^{3+}$ ion ($FeO_6$ octahedra, $FeO_5$ squared pyramids and $FeO_4$ tetrahedra). The existence of these three different $Fe^{3+}$-environments highly impact on the electronic properties of this oxide leading to a narrow band gap. The band structure calculations of the $GdBa_2Ca_2Fe_5O_{13}$ concludes that the $FeO_5$ layers create the CB (conduction band), the $FeO_6$-layers form the VB (valence band) and the $FeO_4$ layers create insulating channels, leading to anisotropic electrical properties that coincide with the experimentally observed 2D magnetic, electrical, and structural characteristics of the $GdBa_2Ca_2Fe_5O_{13}$.

## 1. Introduction

Research on materials oriented towards technological applications is one of the most valuable areas in solid state chemistry and materials science. In this context, metal oxides with perovskite-type crystal structure ($ABO_3$ stoichiometry) constitute prominent archetypes of functional materials, since display an extraordinary wide range of electronic properties.[1] The cubic perovskite structure can be described as a corner-linked $BO_6$-octahedra network with the A-atoms located in 12-coordinated sites formed by four linked octahedra. Transition metal atoms are located at the B-sites while the A-sites are commonly occupied by alkaline-earth metals or lanthanides. The electronic properties of the perovskites are tuned by partial or total substitution of ions into the A and B-sites, sometimes combined by creation of defects such as cation or anion-vacancies. In consequence, metal, insulators and materials with metal-insulator transitions, also presenting noticeable magnetic properties, are found among different perovskite-related families.[2-5] Perovskite-related oxides have gained a great deal of attention in the field of the so-called energy-applications.[6-8] In this regard, numerous perovskites have been studied as electrodes for solid oxide cells, both for fuel cells and electrolyzers (SOFCs and SOECs).[9-14] Particularly interesting are the mixed-conducting non-stoichiometric layered-perovskites, as for instance those of the system $LnBaCo_2O_{6-\delta}$ (Ln = lanthanide metal), with ordering of Ln and Ba in alternated layers along the [001] direction of the structure.[14-19] Layered-type ordering of Ln and Ba in the crystal structure seems to be crucial to the location of the anion vacancies within the $LnO_{1-\delta}$ planes, creating higher ionic conductivity than in perovskites with the anion vacancies placed at random in the structure.[20,21] The high demand of Co-materials for energy applications and the low thermal stability of the $LnBaCo_2O_{6-\delta}$ systems associated to their rapid oxygen release/up-taking makes essential to develop new Co-free perovskites. Substitution of Co by other transition metals in the above mentioned layered-perovskites improves thermal stability, although in general decreases the electronic conductivity, while the ordering in both cationic and anionic sublattices can be modified.[22-24] The ordering of the A-site cations is not only assisted by differences between their ionic radii and oxidation states but also depends on the type and oxidation state of the B-site cations, which highly affect the oxygen content of the compound. Thus, layered-ordering of Gd and Ba in $GdBaMnFeO_{6-\delta}$ is only achieved by using reducing atmosphere in the first step of the synthesis;[25,26] in a similar way, Pr/Ba ordering in $PrBaFe_2O_{6-\delta}$ requires synthesis under reducing conditions.[27]

Coupling of cation and anion-vacancies orderings to form perovskite-based superstructures is clearly perceived in some complex $Fe^{3+}$-perovskites, where the $Fe^{3+}$ cations can adopt different oxygen coordination.[28,29] Thought provoking is the modulation of the nuclear and magnetic structures in the $Ln_{0.8-x}Ba_{0.8}Ca_{0.4+x}Fe_2O_{6-\delta}$ systems (Ln = Gd, Tb).[30,31] Three single-phase oxides

have been isolated in the system, which are better formulated as $Ln_{1.2}Ba_{1.2}Ca_{0.6}Fe_3O_8$, $Ln_{2.2}Ba_{3.2}Ca_{2.5}Fe_8O_{21}$ and $LnBa_2Ca_2Fe_5O_{13}$ (corresponding to x = 0.00, 0.25 and 0.40 respectively) in agreement with their oxygen content; the compounds constitute the $A_{3m+5n}Fe_{3m+5n}O_{8m+13n}$ homologous series with m and n values 1, 0; 1, 1; and 0, 1, respectively. These three complex perovskite-related oxides present different layered-ordering of the A-site cations in combination with different oxygen-coordination environment around the $Fe^{3+}$ atoms (octahedra, tetrahedra and squared pyramids) along the stacking c-axis. In the system, substitution of $Ln^{3+}$ by $Ca^{2+}$ decreases the oxygen content, which is accommodated by formation of $FeO_5$-squared pyramids layers intercalated with one A-layer containing mainly $Ln^{3+}$ cations. Like in the above-mentioned layered Co-perovskites,[20,21] the isolated $Ln^{3+}$ layers might favor the anion conductivity through them, explaining that the $LnBa_2Ca_2Fe_5O_{13}$, with unit cell with the highest isolated $Gd^{3+}$ layers rate in the series, also presents, in addition to the highest electronic conductivity, the best electrocatalytic properties.[30] The antiferromagnetic behavior of these $Fe^{3+}$ containing oxides is also influenced by the ordering and type of oxygen-polyhedra around the Fe atoms, demonstrating, once again, the relation between crystal and electronic properties.[31] Interestingly, the variation of their electrical conductivity with temperature, typical for semiconducting mechanism, shows a smooth transition in a relatively wide range of temperature (between ~ 600 K and ~ 900 K). The electrical transition is coupled with a broad magnetic transition, in the same temperature range, associated with the evolution of 3D into 2D-magnetic behavior.[30,31]

The studies on these complex layered perovskites are primarily focused on their physical properties in connection with their crystal structure, while the electronic structure is scarcely considered. Relatively recent advances in electronic structure theory, in particular density functional theory (DFT), in parallel with the improvements in computing power, allow to explain a great variety of materials properties and predict new compounds with certain thermodynamically stable crystal structure and behavior. We present in here a thorough computational study on the layered-perovskite $GdBa_2Ca_2Fe_5O_{13}$ (GBCFO), a potential oxygen electrode material for SOFCs. The work is focused on determining the electronic structure of the oxide to understand its functional properties and, therefore, to establish adequate relationships between its phase composition, crystal, and electronic characteristics. Among the oxides of the $A_{3m+5n}Fe_{3m+5n}O_{8m+13n}$ series, the $GdBa_2Ca_2Fe_5O_{13}$ presents the highest electronic conductivity and oxygen reduction reaction activity.[30] In addition, the crystal structure of the studied oxide contains three types of oxygen-polyhedra around the $Fe^{3+}$ cations (octahedra, tetrahedra and squared pyramids), which seem to be also associated with its superior properties. The results of the calculations also elucidate the previously observed 2D magnetic nature interplayed with the electrical behavior of the

$GdBa_2Ca_2Fe_5O_{13}$, suggesting new approaches of further comprehensive experimental research in layered perovskites with 2D-behavior.

View Article Online
DOI: 10.1039/D5CP01780G





## 2. Computational methods

All first-principles calculations performed in this work were executed in the VASP program package utilizing U-modified density functional theory (DFT + U).[32] The wave functions of atomic valence electrons $2s^22p^4$ for O, $3s^23p^64s^2$ for Ca, $5s^25p^66s^2$ for Ba, $3p^63d^74s^1$ for Fe and $5s^25p^66s^25d^1$ for Gd were treated with the plane augmented wave (PAW) method; the corresponding states of core electrons and atomic nuclei were evaluated with the program-supplied pseudopotentials. Some calculations implied the use of Gd pseudo-potential that included 4*f*-states explicitly, i.e. the configuration of the valence electrons for Gd atom was $5s^25p^66s^25d^14f^7$. The exchange-correlation functional used is the one proposed by Perdew-Burke-Ernzerhof (PBE) formulated within the general gradient approximation (GGA). In addition, the more recently formulated MetaGGA SCAN functional was also tested.[33] These functionals tend to give an underestimated band-gap energy while hybrid functionals more accurately deal with electron localization, in particular HSE06 ones, which are preferable for periodic solids.[34] However, hybrid functionals are computationally more expensive than semi local methods, and also heavily dependent on the choice of the mixing parameter.[35] A common approach is the Hubbard correction that introduces a $U_{eff}$ in the calculation of systems with strongly localized electrons of d and f types. The correction term in DFT + U was selected by following the simplified scheme proposed by Dudarev et al.[36] It should be stressed that the selection of the $U_{eff}$ parameter for the 3d electronic states of Fe atoms often depends on the desired accuracy of particular property simulation.[37] In this work, the respective value was fixed at 4.0 eV, which has previously provided correct $Fe_2O_3$ to $Fe_3O_4$ reduction enthalpies,[38] as well as reasonable electronic band gaps, crystal structure parameters and oxygen ion migration barriers for perovskite-like ferrites containing $Fe^{3+}$ ions in octahedral, square pyramidal and tetrahedral sites.[37,39] More recently, the insulating character of the $YSr_2Cu_2FeO_7$ compound was well captured when electron correlations were treated by the GGA + *U* approximation using a $U_{eff}$ value of 4.0 eV for both Fe and Cu.[40] Also, the value of $U_{eff} = 4.1$ eV was obtained self-consistently for $Fe^{3+}$ cations with octahedral oxygen coordination.[41] For comparative purposes $U_{eff}$ equal to 6.0 eV, calculated for lanthanides,[42] was also introduced for Gd 4f states in one of the calculations. Due to the presence of ions that possess pronounced magnetic properties (Gd, Fe) in the studied oxide, spin polarization was also considered. The cutoff energy for the plane waves was set to be 520 eV; self-consistency of the solution of Kohn-Sham equations was attained when the total energy difference between two consecutive iteration steps did not exceed $10^{-6}$ eV. The increased precision criterion ($10^{-8}$ eV) was

used for the calculation of the electronic spectra and related properties. All the crystal structures studied were preliminarily relaxed with respect to forces acting on every ion considered. The lattice was supposed to be converged, when the total energy difference between two last steps of structural optimization was less than $10^{-3}$ eV. In addition to that, the energy-volume curve was calculated at 16 different volumes of the GBCFO unit cell; thermal dependence of the respective unit cell volume was assessed using quasiharmonic Debye model.[43]

The crystal structure of the $GdBa_2Ca_2Fe_5O_{13}$ oxide was modelled based on the $\sqrt{2}a_p \times \sqrt{2}a_p \times 10a_p$ unit cell ($a_p$ refers to the lattice parameter of the cubic perovskite), with orthorhombic symmetry (*Imma* space group), that contains 4 formula units and 92 atoms in total. In this work, the unit cell and atomic coordinates obtained from the structural refinement of the isostructural $TbBa_2Ca_2Fe_5O_{13}$ (TBCFO) and $Y_{0.9}Ba_{1.7}Ca_{2.4}Fe_5O_{13}$ (YBCFO) oxides using neutron diffraction data were taken as a reference.[30,31,44-47] The graphic representation of the unit cell is depicted in Fig. 1;[30] the respective unit cell directions in Fig. 1 are given in terms of the symmetry of simple cubic perovskite lattice.[30] Three different magnetic structures (with respect to $Fe^{3+}$ 3d electrons) were considered for the calculations (Fig. 1): one ferromagnetic (FM) and two antiferromagnetic (AFM) orderings: A-AFM and G-AFM.

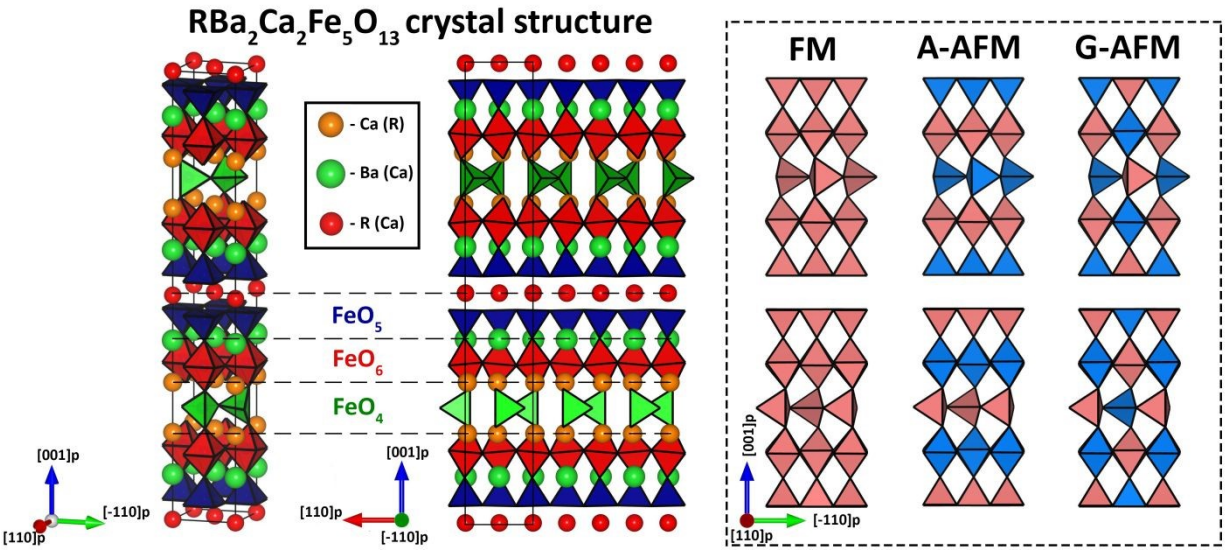


**Figure 1.** Graphic representation of the $RBa_2Ca_2Fe_5O_{13}$ (R= Gd, Tb, Y) crystal structure along different projections and the corresponding magnetic orderings used in this work. Oxygen atoms are not depicted for simplicity. Instead, $Fe^{3+}$-oxygen polyhedra are presented; the corresponding color-coding marks the specific crystalline environment of a particular polyhedron (for the magnetic orderings the color represents the spin state of $Fe^{3+}$ ion located inside; light blue represents spin-down states, light red – spin-up states). Thick black solid line shows the borders of the unit cell, horizontal dashed lines designate the structural layers under consideration. Experimentally observed defects in the ordering of the A-cation sublattice have not been contemplated in the structure.

To assess the thermodynamic stability of various magnetic configurations of the $GdBa_2Ca_2Fe_5O_{13}$ oxide, the total electronic energies of the $Gd_2O_3$, $Fe_2O_3$, BaO and CaO oxides were computed. Defect formation energies in GBCFO were computed for the $2a_p \times 2a_p \times 10a_p$ supercells by utilizing the approach reported earlier.[48] Oxygen interstitials were created by introducing additional oxygen atom in pristine 184-atomic supercell; in turn, oxygen vacancies were made by deleting one of oxygen atoms from it. The scheme of defect allocations used is provided in the supplementary information file.

Total (DOS) and partial (pDOS) density of states spectra of the $GdBa_2Ca_2Fe_5O_{13}$ oxide were computed by utilizing the gaussian smearing method, since the unit cell parameter *c* is almost an order of magnitude larger compared to other typical perovskite unit cell dimensions; accordingly, the k-point sampling of the Brillouin zone (BZ) was selected to be $N \times N \times 1$, where N is a natural number. During the optimization procedure N was taken to be 4, while the electronic properties were calculated assuming $N = 8$. The band centers of mass were computed like in $BaFeO_3$.[49] Intralayer band gaps were estimated based on the position of O 2p and Fe 3d orbitals of oxygen and Fe atoms located in the different layers. Band dispersion was evaluated for the preliminarily optimized GBCFO unit cell under the constraint of preserving orthorhombic symmetry and G-AFM magnetic ordering; the distances between two adjacent high-symmetry points in BZ were interpolated by 25 k-points. Optical spectra were computed via a common approach reported previously.[50] The pre- and postprocessing of the results was accomplished with the vaspkit software.[51] Additional calculations were made for estimating Fe – O bond strength using LOBSTER package.[52]

To study the influence of lattice arrangement of different $FeO_x$ polyhedra on the electronic properties of the resulting compounds, several alternative $Fe^{3+}$-based crystal structures were investigated by the same GGA + U methodology as described above. Namely, orthorhombic $GdFeO_3$, tetragonal $BaCaFe_2O_5$ and hexagonal $CaBaFe_4O_8$ were utilized to represent the contribution solely from $FeO_6$ octahedra, $FeO_5$ square pyramids and $FeO_4$ tetrahedra, respectively. In addition, combinations of two different polyhedra (i.e. $FeO_4$+$FeO_5$; $FeO_4$+$FeO_6$ and $FeO_5$+$FeO_6$) were assessed with the help of $NaCa_2Fe_3O_7$, $GdBaCaFe_3O_8$ and $GdBa_2Fe_3O_8$ orthorhombic crystal structures, which were based on the earlier reported crystal structures.[40] All of the respective calculation details are provided in supplementary information file (Table S1, Figure S1).

The electronic conductivity of the $GdBa_2Ca_2Fe_5O_{13}$ compound was computed with the linearized Boltzmann's transport equation under the constant relaxation time (CRT) approximation using Boltztrap2 software.[53] The input data on band structure were obtained from the self-consistent calculation of G-AFM ordered GBCFO unit cell with the $14 \times 14 \times 2$ k-point sampling

of its BZ (the partial occupancies of orbitals were determined within the tetrahedron method using Blöchl corrections[54]). The electronic conductivity tensor ($\hat{\sigma}_{\mathrm{CRT}}$) was estimated by the following equation:

$$\hat{\sigma}_{\mathrm{CRT}} = \frac{|\bar{e}|^2}{4k_BT}\int_0^{\infty} \Sigma_{\alpha\beta}(E)\left[\cosh\left(\frac{E-E_F}{2k_BT}\right)\right]^{-2} dE \quad (1)$$

where $k_B$ denotes the Boltzmann's constant, $\bar{e}$ – elementary electrical charge, $T$ – absolute temperature, $E$ – energy, $E_F$ – Fermi level and $\Sigma_{\alpha\beta}(E)$ is the so-called transport distribution function which is determined as a sum of integrated tensor products of electron energy derivatives over all bands considered, multiplied by the relaxation time τ:

$$\Sigma_{\alpha\beta}(E) = \frac{\tau}{8\hbar^2\pi^3}\sum_{i=1}^{N_b}\int\left(\frac{\partial E_{i\boldsymbol{k}}}{\partial k_\alpha}\right)\otimes\left(\frac{\partial E_{i\boldsymbol{k}}}{\partial k_\beta}\right)\delta_K(E-E_{i\boldsymbol{k}})d\boldsymbol{k} \quad (2)$$

with $\hbar$ denoting the reduced Planck's constant, $E_{i\boldsymbol{k}}$ the energy of *i*-th band at a specific **k** vector in the reciprocal unit cell and $\delta_K$ is the Kronecker's delta function. The summation in equation (2) is carried out over all $N_b$ bands in the system, while α and β indices designate two distinctive cartesian coordinates of the particular **k** vector. In this work the $\sigma_{\mathrm{CRT}}$ was estimated as a function of temperature and the doping level $p_d$; the latter one was implicitly accounted for in the actual value of Fermi level inserted into equation (1).

## 3. Results and Discussion

### *3.1. Crystal structure and thermodynamic stability of $GdBa_2Ca_2Fe_5O_{13}$*

According to the experimental data, the GBCFO oxide has a highly anisotropic orthorhombic lattice, which can be unambiguously indexed within the $\sqrt{2}a_p \times \sqrt{2}a_p \times 10a_p$ unit cell with *Imma* space group.[30] An important feature of the synthesized $RBa_2Ca_2Fe_5O_{13}$ (R =, Gd, Tb, Y) compounds is the presence of anti-site defects in the A-positions, more noticeable in the case of Y and Ca in the YBCFO.[44,46] However, *ab initio* modeling of such defect compounds implies a complicated computational approach; accordingly, certain approximations allow to achieve reasonable time-to-result ratio. In this work, the A-site disordering in $GdBa_2Ca_2Fe_5O_{13}$ has been modeled by mixing Gd and Ca atoms only in their respective layers. Considering this disordering, three different 92-atomic unit cells were generated with Gd atoms substituting Ca ones and vice versa; the corresponding graphic representations can be found in supplementary (Figure S2). Accordingly, to assess the relative influence of A-site mixing on thermodynamic stability of the *j*-th structural model of the $GdBa_2Ca_2Fe_5O_{13}$ compound, the $\Delta H_{f(j)}$ enthalpy change (i.e. the formation enthalpy) of the following chemical reaction has been computed:

View Article Online
DOI: 10.1039/D5CP01780G

$$\frac{1}{2}Gd_2O_3 + 2BaO + 2CaO + \frac{5}{2}Fe_2O_3 \rightarrow GdBa_2Ca_2Fe_5O_{13}(j)\ (3)$$

The term $j$ in brackets underlines the concrete structural model of the GBCFO used for the calculations. In turn, the $\Delta H_{f(j)}$ quantity can be expressed as:

$$\Delta H_{f(j)} = E^{tot}_{GdBa_2Ca_2Fe_5O_{13}(j)} - \frac{1}{2}E^{tot}_{Gd_2O_3} - 2\left(E^{tot}_{BaO} + E^{tot}_{CaO}\right) - \frac{5}{2}E^{tot}_{Fe_2O_3} + p\Delta V_j (4)$$

where $E_l^{tot}$ denotes the total electronic energy of $l$-th component in the reaction (3), $p$ stands for pressure and $\Delta V_j$ is the overall molar volume change in the $j$-th reaction (3). One should note now that the results of using the formula (4) may strongly depend on the type of magnetic ordering of the GBCFO (all other oxides involved in reaction (3) are assumed to be in their most stable magnetic states at 0 K). Therefore, the calculated formation enthalpies in the framework of GGA + U method are given in Table 1 for both structural disorder and magnetic ordering models in GBCFO.

**Table 1.** The GGA + U computed formation enthalpies of the $GdBa_2Ca_2Fe_5O_{13}$ oxide with different magnetic orderings and A-site mixing models.

| Magnetic ordering | Formation enthalpy, eV | | | |
|---|---|---|---|---|
| | Non-mixed | Model I | Model II | Model III |
| G-AFM | –1.597 | –1.510 | –1.552 | –1.520 |
| A-AFM | –0.820 | –0.729 | –0.776 | –0.745 |
| FM | –0.339 | –0.254 | –0.291 | –0.268 |

As seen, all the estimated $\Delta H_{f(j)}$ parameters are strongly negative, which indicate the thermodynamic preference of the perovskite-like structure over the mixture of binary oxides. Also, one can acknowledge that the anti-site defects in the A-sublattice of GBCFO makes little difference (less than 100 meV) for the resulting $\Delta H_{f(j)}$ value; it is probable, that the small energy gain observed for perfectly ordered GBCFO is counterbalanced by higher entropy of mixing, which eventually enables the stabilization of some Ca atoms within the Gd layer in the GBCFO material. On the contrary, a much more pronounced energy difference is observed for different magnetic orderings. For instance, the calculations revealed that FM and A-AFM structures result in higher $\Delta H_{f(j)}$ values than the G-AFM ordering; the corresponding subtraction gives 1.26 and 0.78 eV/f.u. differences between G-AFM/FM and G-AFM/A-AFM configurations of perfectly ordered GBCFO, respectively. Similar results are achieved for the unit cells with the Gd/Ca mixing (models I, II and III in Table 1). One should note that these outcomes appear to be in general agreement with the Goodenough-Kanamori rules[55] and experimental observations.[31] Accordingly, the G-AFM magnetic structure is proved to be the most stable in the $GdBa_2Ca_2Fe_5O_{13}$ crystalline

View Article Online
DOI: 10.1039/D5CP01780G

framework, disregarding the degree of Gd and Ca mixing; hence, further analysis will be performed only for this type of spin ordering.

Experimental data are a valuable tool for validating the results of $U_{eff}$ corrected GGA (GGA + U) calculations. Indeed, the theoretical unit cell parameters of $GdBa_2Ca_2Fe_5O_{13}$ obtained during structural relaxation (within the G-AFM magnetic ordering) compare with those experimentally determined by X-ray diffraction in the synthesized oxide[23] are in reasonable agreement (Table 2). The very close matching of the GBCFO unit cell volumes estimated by GGA + U and Rietveld methods is especially remarkable; the respective relative difference is less than 0.01 %. The computed energy-volume curve of the G-AFM ordered GBCFO additionally support the computing results – the equilibrium volume at 0 K determined by fitting the respective points with the Birch-Murnaghan equation of state[56] is extremely close to that obtained by simple structural relaxation (see Figure S3(a) in the supplementary information). In addition, the extracted temperature dependence of GBCFO unit cell volume appears to be in good agreement with the experimental observations, Figure S3(b);[57] moreover, the obtained Debye temperature (~430 K at room temperature) coincides well with the known data for similar oxide systems. [58]

**Table 2.** Experimentally determined and DFT + U computed unit cell parameters of $GdBa_2Ca_2Fe_5O_{13}$. Experimental data were taken elsewhere.[30]

| Parameters | Method | | |
|---|---|---|---|
| | Experiment | GGA + U | SCAN + U |
| ***a***, Å | 5.5222 | 5.53056 | 5.49541 |
| ***b***, Å | 5.5625 | 5.58393 | 5.44159 |
| ***c***, Å | 38.309 | 38.106 | 37.375 |
| α, deg | 90 | 90 | 90 |
| β, deg | 90 | 89.991 | 90 |
| γ, deg | 90 | 90 | 90.006 |
| V, Å$^3$ | 1176.75 | 1176.79 | 1117.66 |

On the contrary, the use of SCAN functional in conjunction with the $U_{eff}$ term (SCAN + U) brings worse results – the difference between experimental and computed unit cell volumes of GBCFO is estimated to be ~5 %. Therefore, one may assume that the GGA + U approximation is more precise in terms of estimating the unit cell dimensions. Hence, GGA+U approximation has been used in this work.

Despite the perfect coincidence between GGA + U computed and the experimental unit cell volume of the GBCFO, the respective values of individual unit cell parameters differ significantly although the inconsistencies lie within the typical range of *ab initio* errors.[59] In addition, the structural relaxation of the GBCFO lattice has led to symmetry breaking, thus transforming the initially orthorhombic unit cell with *Imma* space group into the monoclinic $P2_1/n$ one. The

application of SCAN + U approximation has also resulted in the symmetry lowering of the GBCFO lattice, which suggests insufficient precision of structural models used in the calculations (i.e. one does not account for antisite-defects). However, the respective angle deviations from 90° were found to be less than 0.01 in both cases, which implies minor distortion of the GBCFO crystallographic planes.

Although estimation of unit cell dimensions is an important probing for the computational approach, it does not give information on the chemical bonds in the solid. Therefore, it is desirable to compare the calculated bond lengths with those derived from the Rietveld refinement of the structure from the corresponding diffraction data. Since these data are not available in the case of the $GdBa_2Ca_2Fe_5O_{13}$ in the literature, experimental bond lengths of the isostructural compounds $Y_{1.1}Ba_{1.6}Ca_{2.3}Fe_5O_{13}$ and $TbBa_2Ca_2Fe_5O_{13}$ will be used in this work.[31,45] The respective bond lengths and angle distributions calculated by the GGA + U method for GBCFO are given in Table 3 (the atomic coordinates obtained can be found in Table S2 in supplementary file).

**Table 3.** Computed interatomic distances and in-plane bond angles for G-AFM GBCFO in comparison with the corresponding experimental data determined for the $Y_{1.1}Ba_{1.6}Ca_{2.3}Fe_5O_{13}$ and $TbBa_2Ca_2Fe_5O_{13}$ oxides.[31,45] GGA + U derived bond lengths in different $Fe^{3+}$-O polyhedra were preliminarily averaged.

| **Bond distances (Å) and angles (deg.)** | Experimental | | GGA + U |
|---|---|---|---|
| | R = Y | R = Tb | R = Gd |
| **$FeO_6$** | | | |
| **$d_{Fe-O}$ *apical*** | 2.1089 | 2.1332 | 2.1187 |
| | 2.0824 | 2.032 | 2.1187 |
| **$d_{Fe-O}$ *equatorial*** | 1.9462 | 1.9559 | 1.9640 |
| | 1.9462 | 1.9559 | 1.9640 |
| | 1.9684 | 1.9667 | 1.9870 |
| | 1.9684 | 1.9667 | 1.9870 |
| **$FeO_5$** | | | |
| **$d_{Fe-O}$ *apical*** | 1.8718 | 1.9234 | 1.8610 |
| **$d_{Fe-O}$ *equatorial*** | 2.0127 | 1.9958 | 2.0201 |
| | 2.0127 | 1.9958 | 2.0201 |
| | 2.0031 | 1.9915 | 2.0170 |
| | 2.0031 | 1.9915 | 2.0170 |
| **$FeO_4$** | | | |
| **$d_{Fe-O}$ *apical*** | 1.8686 | 1.7532 | 1.8410 |
| | 1.8686 | 1.7532 | 1.8410 |
| **$d_{Fe-O}$ *equatorial*** | 1.8556 | 1.8572 | 1.9230 |
| | 1.9425 | 2.249 | 1.9230 |
| **$d_{Fe-Fe}$ (R layer), Å** | 3.7691 | 3.724 | 3.7692 |
| **$\Theta_{Fe-O-Fe}$ ($FeO_6$)** | 168.94 | 166.77 | 171.66 |
| **$\Theta_{Fe-O-Fe}$ ($FeO_5$)** | 149.34 | 155.58 | 151.41 |

| | | | |
|---|---|---|---|
| **$\Theta_{Fe\text{-}O\text{-}Fe}$ ($FeO_4$)** | 125.06 | 117.88 | 123.96 |

View Article Online
DOI: 10.1039/D5CP01780G

The overall agreement between the experimental bonding distances and angles, and the DFT + U computed values for the GBCFO is satisfactory. The most noticeable difference in the two datasets presented is linked with the geometry of $FeO_4$ tetrahedra: *ab initio* calculations predict more symmetric distribution of Fe–O bond lengths, both in the apical and equatorial positions of the oxygen-atoms. Contrary to that, experimental data of YBCFO and TBCFO show different equatorial Fe–O distances. Still, the degree of mismatch does not exceed 1 % in most cases, thus suggesting an appropriate level of theoretical approximations used. In addition, it should be mentioned that the derived bulk modulus, $B_0$, of the GBCFO (Figure S3(a)) agrees with the one measured for $Fe^{3+}$ containing ferrites that simultaneously contain $FeO_6$ octahedra and $FeO_4$ tetrahedra in the structure with ~1.8 Å and ~2.0 Å Fe–O bond lengths respectively.[60] When only $FeO_6$ octahedra are present, the $B_0$ magnitude is usually higher.[61] Finally, it must be stated that the in-plane Fe–O–Fe bond angles for the different oxygen-polyhedra around the $Fe^{3+}$-cations in RBCFO are significantly different, which is well reproduced by the GGA + U method. This observation suggests that the degree of overlap between Fe-orbitals and O-orbitals differs depending on the coordination number of the $Fe^{3+}$ cations. Hence, individual contributions from the respective 3d electronic states to DOS might vary depending on the type of $Fe^{3+}$–O polyhedron, like it has already been reported for the YBCFO.[45]

### *3.2.Electronic band structure & chemical bonding of $GdBa_2Ca_2Fe_5O_{13}$*

Prior to discussing the electronic structure of the studied compound, it is instructive to note that Gd is a 4f-element. Therefore, the presence of 4f-electrons might render certain influence on the resulting electron density. However, it is often assumed that in the vicinity of Fermi level, the electronic states are essentially independent on the respective 4f-states in the rare-earth containing crystals.[62] This is also known as the frozen-core approximation.[63] With the aim to examine whether the Gd 4*f* electrons can indeed influence the DOS of the GBCFO, a separate calculation was made involving the previously studied $GdFeO_3$ oxide as a test compound. The actual calculations made for the G-AFM $GdFeO_3$ with and without frozen-core approximation have shown that the obtained $E_g$ values are similar, corresponding to 2.421 and 2.412 eV respectively, see Figure S4 in supplementary file. It should be noted that both results fall into the experimentally determined $GdFeO_3$ band gap range of 2.1 – 2.5 eV;[64] moreover, they are almost indistinguishable from each other. In addition, the computed distribution of Fe and O electronic states within the bands for both approaches used appears to be the same in the vicinity of Fermi level (Figure S4). The obtained result is reasonable, as the corresponding Gd 4*f* states were found to lie ~5.5 eV beneath the top

of the valence band (VB), (Figure S4); accordingly, their influence on the Fe and/or O states should be insignificant. The reported numerical estimations of magnetic interactions fully support this conclusion.[64] Hence, the frozen core approximation can accurately be utilized for treating the electronic structure of the GBCFO oxide.

The computed DOS spectrum under the GGA + U approximation of the GBCFO oxide is presented in Fig. 2(a).

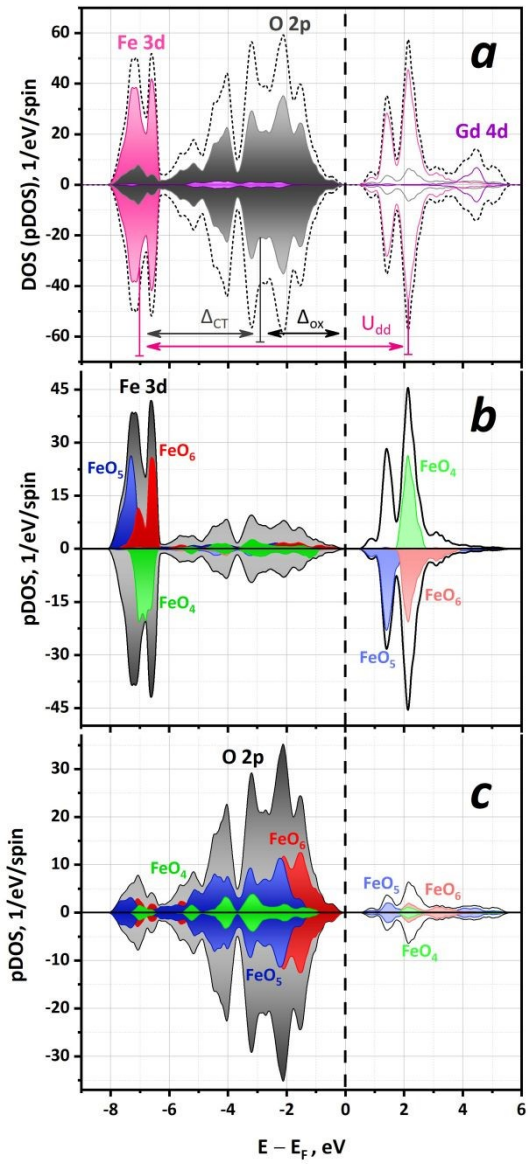


**Figure 2.** The GGA + U computed electronic spectra of $GdBa_2Ca_2Fe_5O_{13}$. **(*a*)** The total DOS (dotted line) and pDOS (filled areas/solid lines) curves evaluated for all Gd, Fe and O atoms in GBCFO (filled areas show filled states, solid lines above the Fermi level designate empty states). **(*b*)** pDOS of the Fe-sublattice in GBFCO (filled grey area/black solid line) and respective partial contributions from $Fe^{3+}$ cations located in different oxygen polyhedra (filled colored areas); lighter colors correspond to empty states. **(*c*)** pDOS of the O-sublattice (filled grey area/black solid line) and respective partial contributions from oxygen ions located in layers belonging to different oxygen polyhedral around the $Fe^{3+}$ ions (filled colored areas); non-colored areas correspond to empty states. Negative values designate spin down states. The vertical dashed line

shows the position of the Fermi level. The type of polyhedron associated with a certain pDOS, is also marked on the figure.

View Article Online
DOI: 10.1039/D5CP01780G





The results indicate that the studied compound is a narrow-gap semiconductor with a band gap value of $E_g = 0.53$ eV. The corresponding estimation of partial contributions to DOS reveal typical particularities for $Fe^{3+}$ containing perovskites – the severely spin-splitted Fe 3d band, part of which is forming the bottom of the conduction band (CB) and a wide O 2p band providing the top of the VB.[64-67] One can also acknowledge the overlying Gd 4d states (~4 eV above the bottom of the CB) which are too high in energy to participate in the electron conduction process. Accordingly, the electronic structure of the GBCFO, in general, represents the common picture of localized electrons in a transition metal oxide.[49]

However, the implication of the layered crystalline architecture causes some peculiarities to appear in the DOS spectrum. Namely, the distribution of electronic states for Fe and O atoms was shown to depend on $Fe^{3+}$-environment in the unit cell, in particular on the exact type of oxygen-polyhedron around the $Fe^{3+}$ cations. The mentioned data are shown in more detail in Fig. 2(b) and 2(c) for Fe 3d and O 2p states, respectively. Considering the information presented in Fig. 2(b) one can notice the wide low-intensity Fe band ranging from –6 eV up to the Fermi level; these are the Fe 3d – O 2p hybridized states. At the same time, peak-shaped Fe 3d states located both in the VB and in the CB are split with the lower energy peak corresponding to pyramidally coordinated Fe atoms. In turn, higher energy states are provided by a combination of electrons bound to the Fe atoms located in $FeO_4$ tetrahedra and $FeO_6$ octahedra. Given the large splitting energy ( > 1 eV), it is concluded that the $FeO_5$ layers are mainly responsible for the formation of the CB in GBCFO. On the other hand, the pDOS of the O 2p states in equatorial oxygen positions of the different polyhedron (i.e. $FeO_4$ tetrahedron, $FeO_5$ square pyramid or $FeO_6$ octahedron) shows that the top of the VB is also spatially specific (Fig. 2(c)). Namely, only those states that belong to equatorial oxygen atoms located in $FeO_6$ octahedra do contribute to the top of VB. The states of oxygen ions in $FeO_4$ and $FeO_5$ polyhedra appear to be ~ 1 eV lower in energy and hence their influence on electrical transport properties can be neglected. Accordingly, GBCFO may be considered as a 2D-semiconductor with $FeO_5$-layers acting as CB, $FeO_6$-layers as VB and $FeO_4$ ones as effectively insulating channels. This result seems to be controversial, as a previous report in the isostructural YBCFO suggested the top of VB is in the $FeO_4$-layer.[45] Still, the use of other functionals (i.e. SCAN) in this work gives similar distribution of the electronic states.

It is important to notice that the computed band gap value (0.53 eV) for the GBCFO is unusually small in comparison with the other $Fe^{3+}$-perovskites.[60,68,69] Considering the relation between electric bandgap and optical bandgap, we have calculated the optical spectrum of the

G-AFM GBCFO, see Figure S5 in supplementary file. The color of the solid can be estimated theoretically from its reflectance spectrum.[70] The one of the GBCFO (Figure S5) shows that its reflectance is approximately constant in the visible range; the respectively estimated CIE-color[71] is dark brown in agreement with the experimental color of the studied oxide,[30] although the determined band gap suggests the material should be totally black.[70] This counterintuitive result originates from the peculiar band dispersion in GBCFO – the calculated energy band diagram (Figure S6 in supplementary file) indicates that the band gap in the studied compound is indirect in nature and hence the relative contribution of the electronic transition to the overall light absorption should be small. On the contrary, strongest impact on optical absorption is provided by direct transitions, which are higher in energy (above 2 eV). Consequently, the intense increase of optical absorbance in GBCFO is observed only at UV wavelengths, which explains the non-black color of the material considered.

Although the DOS spectra provide important information about the electronic structure, do not allow to estimate the spatial localization of bands, which is of special importance for semiconductors. Figure 3 displays the calculated electron charge densities in CB and VB projected onto specific crystallographic planes of the GBCFO structure.

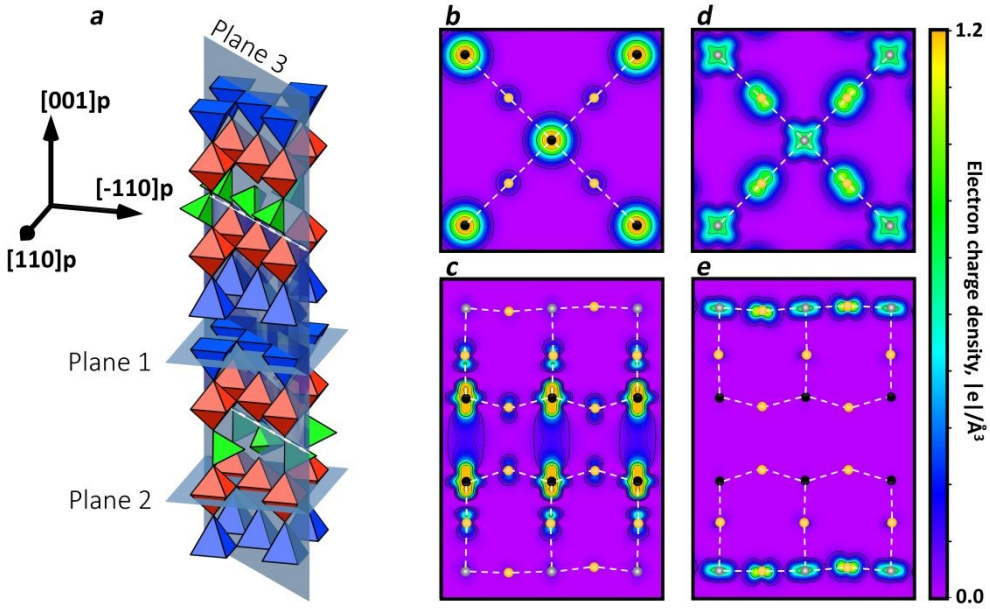


**Figure 3.** Graphical representation of the crystal structure of $GdBa_2Ca_2Fe_5O_{13}$ (*a*); the corresponding representation omits the A-site cations and oxygen anions for simplicity – only oxygen polyhedra around $Fe^{3+}$ cations are shown. The GGA + U computed charge densities of electrons in the conduction (*b* and *c*) and valence (*d* and *e*) bands of GBCFO, projected onto specific crystallographic planes. The respective planes are schematically shown in panel (*a*) as rectangles that cross-section the unit cell of GBCFO. Panel (b) corresponds to charge density projected onto plane 1, panel (*c*) – onto plane 3, panel (*d*) – onto plane 2 and panel (*e*) represents electron density projected onto plane 3. Panels (*c*) and (*e*) show the charge density projections along the $[001]_p$ direction; the respective span range is marked on plane 3 by white solid lines

(*a*). The presented charge density maps (*b*, *c*, *d* and *e*) also contain the positions of Fe atoms resting in $FeO_6$ octahedra (shown as grey spheres) and in $FeO_5$ pyramids (shown as black spheres). Oxygen sites are also marked as bright yellow spheres along with the respective Fe–O bonds (dashed white lines).

View Article Online DOI: 10.1039/D5CP01780G

The spatial distribution of charge within the CB and VB is significantly different. The charge distribution in the CB is revealed to be essentially localized on Fe atoms located in the $FeO_5$ square pyramids, while in the VB the charge is more delocalized with comparable contributions of the Fe atoms and equatorial oxygens of the $FeO_6$ octahedra. These findings fully coincide with the conclusions derived from the DOS/pDOS spectra (Figure 2). Importantly, both bands show pronounced anisotropy of the charge distribution – they appear to be concentrated mainly in the quasi-2D layers perpendicular to the *c*-axis ($[001]_p$ direction), see Figure S7 in supplementary. in agreement with the evaluated band dispersions (Figure S6). The analysis of different projections of charge density in the CB, Figs. 3(*b*) and 3(*c*), indicates the conducting states are mainly formed by $d_{3z^2-r^2}$ Fe orbitals. The VB shows Fe 3d – O 2p hybridized behavior of the $d_{x^2-y^2}$ Fe states, Figs. 3(*d*) and 3(*e*). It should be stated that the derived picture of charge distribution in conjunction with the observed band curvatures (Figure S6) suggests that the electronic transport in the CB should be more localized than in the VB in agreement with earlier studies in other $Fe^{3+}$-perovskites.[37,72,73]

The unique existence of the three different types of $Fe^{3+}$-environment in the crystal structure makes the RBCFO (R = Y, Gd, Tb) oxides interesting playground for testing the influence of the oxygen coordination of $Fe^{3+}$ cations on their complete electronic behavior. In this sense, the NPD experiments on TBCFO revealed different magnetic moments localized on $Fe^{3+}$ ions ($\mu_{Fe}$) depending on their oxygen coordination.[31] The calculated data for GBCFO and the experimental values determined for TBCFO are compared in Table 4.

**Table 4.** Calculated electronic parameters of the GBCFO oxide. $U_{dd}$ is the magnitude of splitting of the Fe 3d states, $\Delta_{CT}$ is the charge transfer energy, $\Delta_{ox}$ is the average amount of energy required to transfer electron from the O-2p band to the top of the VB. The presented data are associated to the oxygen environment of the Fe atoms. The numbers in brackets in the top row represent the experimental values obtained for TBCFO.[24]

| Parameters (eV) | Crystallographic environment | | | |
|---|---|---|---|---|
| | Tot | $FeO_6$ | $FeO_5$ | $FeO_4$ |
| $\lvert\mu_{Fe}\rvert$, $\mu_B$ | 0.0 (0.0) | 4.09 (3.9) | 4.04 (3.8) | 4.05 (3.0) |
| $E_g$ | 0.53 (0.38*) | 1.90 (2.4**) | 1.67 (1.35**) | 2.79 (3.02**) |
| $U_{dd}$ | +9.05 | +9.16 | +8.7 | +9.05 |
| $\Delta_{CT}$ | –4.08 | –3.83 | –3.73 | –3.63 |

| | | | | |
|---|---|---|---|---|
| $\Delta_{ox}$ | +2.93 | +2.93 | +3.41 | +3.23 |



** - the value is estimated from the temperature dependence of the GBCFO conductivity[23]*

*** - the band gaps are obtained for the compounds with only one type of $FeO_x$ polyhedron*

Regarding the individual magnetic moments, GGA + U calculations give correct (within the 6 % error limit) values for Fe atoms located in the $FeO_5$ square pyramids and $FeO_6$ octahedra but fail to predict the significant decrease of the $\mu_{Fe}$ in $FeO_4$ tetrahedra. It is important to notice that a similar issue was detected for the $Ca_2Fe_2O_5$ brownmillerite where the experimentally observed difference between the $\mu_{Fe}$ in $FeO_4$ and $FeO_6$ polyhedra[74] was not properly reproduced by DFT + U calculations.[66] Nevertheless, the detailed analysis of the pDOS spectra of GBCFO has shown that the electronic states in $FeO_4$ layers do not contribute to VB and CB edges and hence the improper $\mu_{Fe}$ values cannot be considered as substantial incorrectness of the calculation method.

As follows from the data presented in Table 4, the partial $E_g$ values are significantly higher (if compared to the total $E_g$) for each polyhedron type but $E_g$ is especially large in the case of the $FeO_4$ tetrahedra (~2.8 eV), assuming these sites form insulating layers in GBCFO lattice. Notably, a very close band gap is obtained for $CaBaFe_4O_8$ that contains entirely $FeO_4$ structural units in its lattice, see Figure S8(a); this result is also supported by the respective optical measurements (Figure S8(b)). In addition, the computed $E_g$ values for $GdFeO_3$ and $BaCaFe_2O_5$ oxides (Figure S9 in supplementary file) that contain only $FeO_6$ and $FeO_5$ structural units respectively, were found to be in qualitative coincidence with the data obtained for individual $FeO_6$ and $FeO_5$ layers in GBCFO, see Table 4. Considering all the above results, one can suppose that the combination of $FeO_4$, $FeO_5$ and $FeO_6$ polyhedra in one lattice provides synergetic effect on the outcoming electronic band structure.

To support this conclusion, it is important to study the implications in the band structure due to the elimination of one of the types of the $FeO_x$ polyhedra. In this context, another compound of the $A_{3m+5n}Fe_{3m+5n}O_{8m+13n}$ series was studied, the $Gd_{1.2}Ba_{1.2}Ca_{0.6}Fe_3O_8$, which contains only $FeO_4$ tetrahedra and $FeO_6$ octahedra.[30] The calculation was made for the perfectly ordered $GdBaCaFe_3O_8$. The GGA + U computed DOS/pDOS spectra for the $GdBaCaFe_3O_8$ oxide are presented in Figure 4(a) (the corresponding representation of the unit cell is given in the inset[30]).

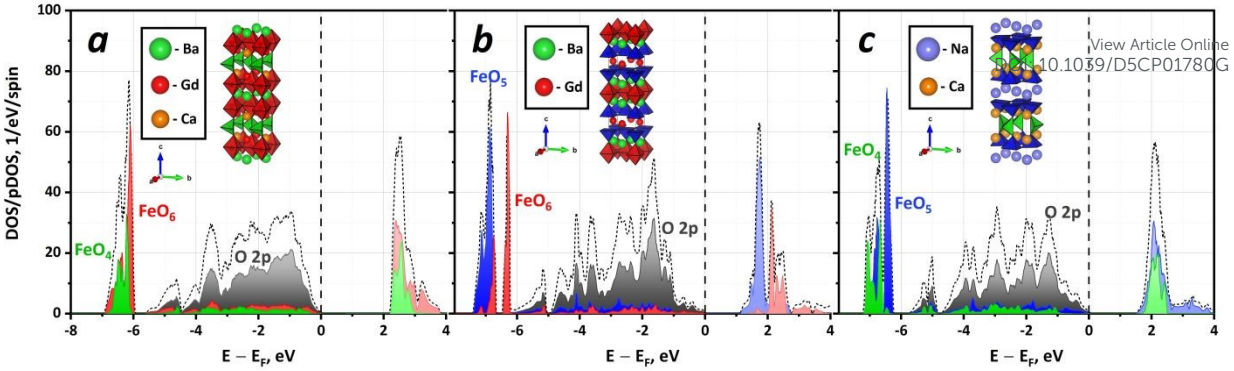


**Figure 4.** DOS spectra (dashed lines) of $GdBaCaFe_3O_8$ (a), $GdBa_2Fe_3O_8$ (b) and $NaCa_2Fe_3O_7$ (c) oxides calculated with the GGA + U method. Colored areas depict the pDOS of Fe 3d states computed for Fe atoms located in octahedra (red color), square pyramids (blue color) and tetrahedra (green color). The spin-down states are not shown as they are fully symmetrical to the spin-up ones. The vertical dashed lines show the position of the Fermi level. The insets depict graphic representations of the crystal structures of the respective compounds.

In this case, the Fe-3d levels in the CB and the VB show similar positioning on the energy scale, disregarding the actual $FeO_x$ polyhedron type, which differs from the spectrum of the $GdBa_2Ca_2Fe_5O_{13}$. In addition, the band gap of $GdBaCaFe_3O_8$ is estimated to be ~ 2.2 eV, thus falling in the typical range of $E_g$ values of $Fe^{3+}$-perovskites.[68,69]

Another possibility is the combination of either $FeO_5$ square pyramids and $FeO_6$ polyhedra, or $FeO_5$ pyramids and $FeO_4$ tetrahedra. These combinations containing only $Fe^{3+}$ ions can be modeled by $GdBa_2Fe_3O_8$ and $NaCa_2Fe_3O_7$ structures, respectively. Although these compounds have not been reported experimentally, the corresponding unit cells were built based on the known structures of $YSr_2Cu_2FeO_8$ and $YSr_2Cu_2FeO_7$ [40], which resemble in certain sense the GBCFO lattice. The computed DOS/pDOS spectra of $GdBa_2Fe_3O_8$ and $NaCa_2Fe_3O_7$ are presented in Figures 4(b) and 4(c), respectively. As seen, the copresence of $FeO_6$ and $FeO_5$ polyhedra brings the lowest band gap of ~ 1.1 eV; importantly, this result corroborates with the noticeable splitting of Fe 3d states in the CB of $GdBa_2Fe_3O_8$ among the respective polyhedra, Figure 4(b). In turn, the combination of $FeO_4$ tetrahedra and $FeO_5$ pyramids provides a band gap of ~ 1.6 eV, Figure 4(c), which is in between of $E_g$ values obtained for $GdBa_2Fe_3O_8$ and $GdBaCaFe_3O_8$. Interestingly, bringing two different types of $FeO_x$ polyhedra in one lattice allows for certain $E_g$ reduction, if compared to the case of crystals that have only octahedra ($E_g$ = 2.41 eV), only square pyramids ($E_g$ = 1.35 eV) or only tetrahedra ($E_g$ = 3.02 eV). Still, none of the double combinations provides as much band gap contraction as is observed in the GBCFO case. Therefore, it seems that the co-presence of all the three $FeO_x$ structural units discussed is indeed required to obtain a narrow band gap in $Fe^{3+}$ containing perovskite-like compounds. The schematical depiction of the observed peculiarity is shown in Figure 5.

View Article Online
DOI: 10.1039/D5CP01780G



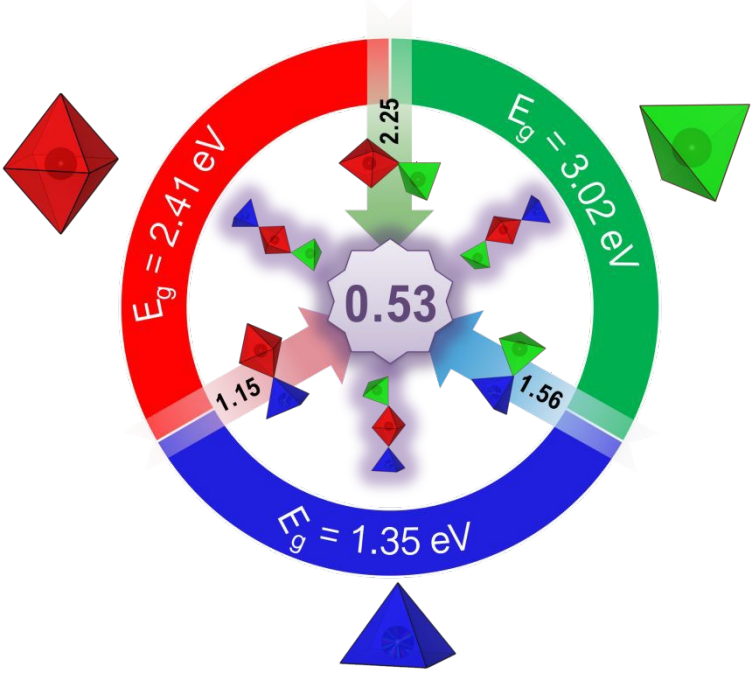


**Figure 5.** Graphic representation of the influence of different combinations of $FeO_x$ polyhedra on the band gap of perovskite-related lattices.

The obtained DOS of GBCFO (Figure 2) allows to elucidate other important band structure parameters, also collected in Table 4: $U_{dd}$, the magnitude of splitting of the Fe 3d states; $\Delta_{CT}$, the so-called charge transfer energy; and $\Delta_{ox}$ – the average amount of energy required to transfer electron from the O-2p band to the top of VB.[49] The magnitude of these parameters is schematically shown in Fig. 2(a). Determination of the respective band centers, which can be done using multiple ways, must be carried out to compute $U_{dd}$, $\Delta_{CT}$ and $\Delta_{ox}$. In this work, it was assumed that the band center of the Fe-related states should not include those located in a wide Fe 3d – O 2p hybridized band; in turn, similar approach was utilized for the O-2p states that contribute to Fe-3d peaks placed deep in the VB and CB. The calculated values suggest that the studied compound is a negative charge transfer oxide, which is characteristic of $Fe^{3+}$-perovskite-type oxides.[49] The high magnitude of $U_{dd}$ energy ( > 9 eV) provides strong evidence that under oxidation of GBCFO, the increased charge will be accumulated on oxygen sites.[47] In turn, the large $\Delta_{ox}$ parameter ( ~3 eV) implies high energy required for oxygen vacancy formation in GBCFO, which is indeed experimentally observed.[30,44] Therefore, one can acknowledge the sufficient precision of GGA + U approximation utilized in this work, capable of reproducing the key experimental findings reported previously.

Considering the essential differences in the computed pDOS spectra between the alternating layers with different Fe-environments in GBCFO, individual estimation of $U_{dd}$, $\Delta_{CT}$ and $\Delta_{ox}$ for these layers makes certain sense. The respective data for $FeO_4$-, $FeO_5$- and $FeO_6$-containing layers

are given in Table 4 (importantly, the discussed estimation of band structure parameters did not involve apical oxygen sites but only equatorial ones). The charge transfer energy remains essentially the same disregarding the polyhedron type, which means that the electrons transferred from any Fe site in GBCFO will be immediately replaced (with approximately the same speed) by other electron from the O-2p formed VB. However, the magnitude of the $U_{dd}$ energy is slightly lower for the Fe atoms in the $FeO_5$ square pyramids. Apparently, this observation may be responsible for the revealed particularity of CB formation in the GBCFO. In accord with that, the lowest $\Delta_{ox}$ value is calculated for $FeO_6$-containing layers, thus explaining why these d-orbitals form the top of the VB.

A certain alignment with the previously discussed data can be found in the LOBSTER computed partial Crystal Orbital Hamilton Population (pCOHP) curves, which basically show the bonding (if pCOHP < 0), non-bonding (pCOHP = 0) or antibonding (when pCOHP > 0) character of the chemical interactions.[52] The respectively estimated pCOHP curves for the Fe–O bonds in the different oxygen coordination polyhedra of GBCFO lattice are shown in Figure 6. The results indicate that chemical interaction between Fe and oxygen atoms shows strongly bonding character deep in the VB (< –6 eV) disregarding the type of polyhedron, apical or equatorial allocation of the oxygen ions and $Fe^{3+}$ spin state. This conclusion agrees with previous findings in $BaFeO_3$.[49] Similarly, pCOHP values become positive in the CB of the GBCFO for all considered cases, which marks the anti-bonding character of the interactions and hence the excited nature of these states. Interestingly, the bonding type between Fe-3d and O-2p electrons in the upper part of the VB (i.e. in the energy range from –6 to 0 eV) is found to be spin-dependent: spin-up electrons of Fe atoms form bonding type interaction, while the inverse process is observed for spin-down electrons. As discussed previously,[49] this observation comes from the inversion of the respective contributions of 3d and 2p orbitals to the Fe–O chemical bond depending on the spin state of the 3d electrons. In this sense, the type of oxygen polyhedron around the Fe atoms should not change that picture, which is indeed observed in the case of GBCFO. However, the shape and relative position on the energy scale of a certain pCOHP are shown to be highly dependent on the Fe-coordination. For instance, the anti-bonding Fe–O states in the CB, that belong to $FeO_5$ square pyramids are located much closer to the Fermi level in comparison with the $FeO_4$ or $FeO_6$ cases (Figure 6(*b*)). The anti-bonding interactions between Fe and O atoms observed at the top of the VB correspond to the $FeO_6$ octahedra, (Figure 6(*a*)). Finally, in the case of $FeO_4$ tetrahedra, the character of chemical interaction appears to be non-bonding in the vicinity of the Fermi level. All the above results suggest that the excited electronic states in the GBCFO tend to localize either in $FeO_5$ layers (when considering electrons in CB) or in $FeO_6$ ones (when implying electron holes in VB). At the same

time, those states located in $FeO_4$ layers can be considered as effectively insulating (Figure 6(*c*)) in complete agreement with the conclusions derived from the DOS data.

View Article Online
DOI: 10.1039/D5CP01780G





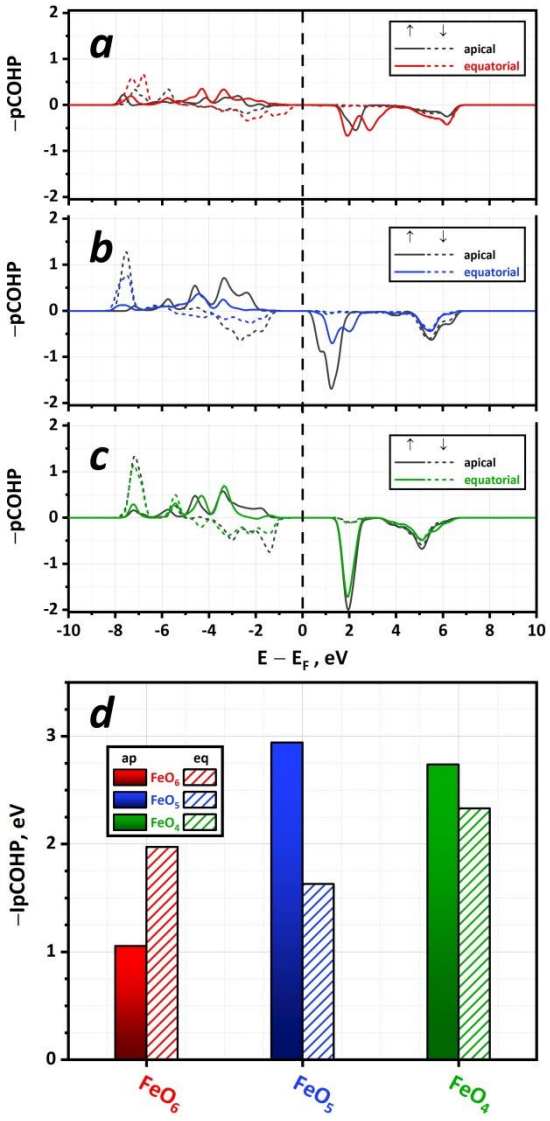


**Figure 6.** The LOBSTER computed pCOHP curves for Fe–O bonds in $FeO_6$ octahedra (*a*), $FeO_5$ square pyramids (*b*) and $FeO_4$ tetrahedra (*c*) of GBCFO. Solid lines show spin-up contributions and dotted lines spin-down ones. Colored lines correspond to Fe–O bonding of oxygen in equatorial sites. The Fermi level position is marked with a vertical dashed line. The respectively obtained IpCOHP values are presented in panel (*d*). The data on both spin channels were summed up for each bar. Filled bars show IpCOHP between apical oxygens and Fe, the hatched ones depict IpCOHP between equatorial oxygens and Fe atom.

An essential information about the chemical bond strength can be obtained by the integration up to the Fermi level of the pCOHP curves (IpCOHP). These data quantitatively measure the energy of covalent bonds in eV units;[52] it can be often used as a guideline for searching the most probable defect configurations in non-stoichiometric oxides.[49,75] The respective results for Fe–O

bonds in GBCFO are presented in Figure 6(*d*). All computed IpCOHP values are negative, which marks the essential chemical stability of $Fe^{3+}$- perovskites. However, the magnitude of |IpCOHP| differs drastically depending on the Fe-coordination. In particular, the magnitude of IpCOHP for the apical oxygens and Fe atoms located in $FeO_6$ octahedra indicates low bond strength. Contrary to that, in the case of other $FeO_x$ polyhedra, the respective quantity significantly increases, thus suggesting that apical oxygen ions are much stronger bonded to $FeO_4$ tetrahedra and $FeO_5$ square pyramids. It should be noted that this conclusion nicely coincides with the GBCFO bond lengths presented in Table 3 – the shorter is the bond, the stronger the bonding and vice versa. Accordingly, one can expect that apical oxygen sites of the $FeO_5$-units are unlikely to become vacant. On the contrary, the equatorial positions have other distribution of IpCOHP energies with the highest one belonging to Fe–O bonds located in $FeO_5$ square pyramids, suggesting that these positions are the most probable sites for oxygen vacancy formation. However, one should consider that the largest (among other polyhedra) $\Delta_{ox}$ value in $FeO_5$ (see Table 4) implies higher energies to transfer electrons from the hybridized Fe 3d – O 2p band to the Fermi level. Hence, one may expect the decreased |IpCOHP| value in case of $FeO_5$ pyramids as evidence of Fe–O bond extension induced by the absence of apical oxygen atoms in the Gd layer. Accordingly, the most probable place for oxygen vacancy formation in GBCFO is the equatorial O sites in $FeO_6$ octahedra.

### *3.3 Electronic conduction behavior of $GdBa_2Ca_2Fe_5O_{13}$*

The studied compound has a crystal structure that induces a highly anisotropic magnetic behavior.[24] In this sense, the band structure of the GBCFO reveals pronounced 2D character of the electronic states' distribution. This result implies that the electronic conductivity of the GBCFO should be dependent on the direction of the applied electric field propagation. Considering that the crystalline lattice of GBCFO has orthorhombic symmetry, and considering the crystallographic directions of the cubic perovskite structure, one can write its electronic conductivity tensor $\hat{\sigma}_{el}$ as:

$$\hat{\sigma}_{el} = \begin{bmatrix} \sigma_{el}||[110]_{\mathrm{p}} & 0 & 0 \\ 0 & \sigma_{el}||[-110]_{\mathrm{p}} & 0 \\ 0 & 0 & \sigma_{el}||[001]_{\mathrm{p}} \end{bmatrix} \quad (5)$$

where $\sigma_{el}||[110]_{\mathrm{p}}$, $\sigma_{el}||[-110]_{\mathrm{p}}$and $\sigma_{el}||[001]_{\mathrm{p}}$ denote individual contributions, being parallel to the $[110]_p$, $[-110]_p$ and $[001]_p$ crystallographic directions respectively (see Figure 1 for more details). Equation (5) suggests that measuring conductivity in different directions of a GBCFO single crystal, the exact values of each $\hat{\sigma}_{el}$ tensor component can be determined. However, the available experimental data correspond to a polycrystalline sample, which makes direct comparison with equation (5) difficult. To overcome this problem one can assume that the GBCFO grains are small enough to be randomly oriented in the sample studied. Then, the experimental

View Article Online
DOI: 10.1039/D5CP01780G

conductivity $\sigma_{exp}$ can be expressed as a normalized trace of $\hat{\sigma}_{el}$ which yields the following simple result:

$$\sigma_{exp} = \langle \hat{\sigma}_{el} \rangle = \frac{\sigma_{el}||[110]_{\mathrm{p}} + \sigma_{el}||[-110]_{\mathrm{p}} + \sigma_{el}||[001]_{\mathrm{p}}}{3} \quad (6)$$

where angular brackets denote the averaging procedure. Accordingly, the direct comparison between computed $\langle \hat{\sigma}_{\mathrm{CRT}} \rangle$ and measured $\sigma_{exp}$[30] becomes possible; the respective data are given in Figure 7.

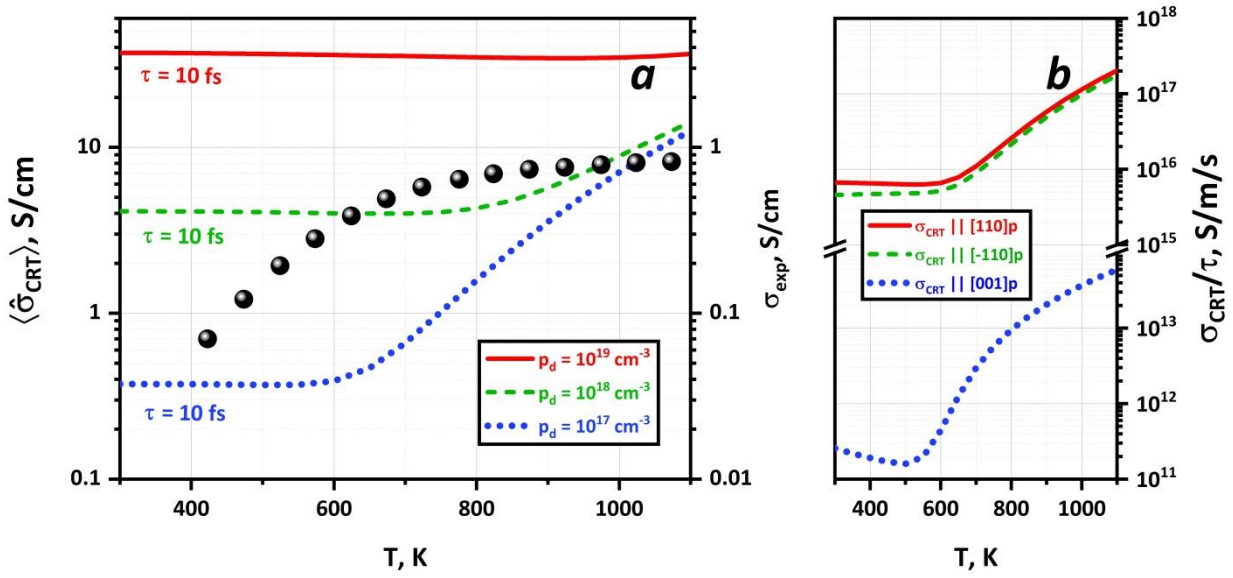


**Figure 7.** The calculated (lines) and experimentally measured (points) electronic conductivity of polycrystalline GBCFO vs. temperature (*a*). The numerical values of $\langle \hat{\sigma}_{\mathrm{CRT}} \rangle$ are obtained assuming $\tau$ = 10 fs; the influence of different doping level $p_d$ is also accounted for. Theoretically computed $\sigma_{\mathrm{CRT}}/\tau$ functions being parallel to different directions of GBCFO lattice vs. temperature (*b*). The doping level for each curve is taken to be $p_d = 10^{17}$ cm$^{-3}$.

It is worth mentioning that the CRT approach used in this work does not allow to properly estimate the magnitude of relaxation time $\tau$. However, the previously published results suggest this parameter lies within the range of few dozens of femtoseconds ($10^{-15}$ sec).[76] Therefore, one can assume $\tau$ = 10 fs for the GBCFO, which agrees with the independently evaluated $\tau$ for the donor-doped $SrTiO_3$ perovskite.[73]

Prior to discussing the peculiarities of transport phenomena in the studied material it is instructive to provide brief description of its defect structure; the respective information allows to elucidate the concentration of charge carriers in the VB and CB, which is of primary importance for electronic conductivity calculations. Given that GBCFO is a narrow band-gap semiconductor it is necessary to account for different extrinsic processes of defect formation, as well as for the intrinsic thermal ionization. For instance, one can suppose that oxygen incorporation can occur into the different structural vacancies in the GBCFO lattice, i.e. into $FeO_5$ or $FeO_4$ layers, thus

producing interstitial sites $O_i$. Another possibility is that oxygen vacancies $V_O$ can be formed – these can be located in all $FeO_x$ polyhedra. The list of possible sites for hosting defects, as well as the corresponding defect formation reactions are given in the supplementary information file. The results of GGA + U calculations of the j-th defect formation enthalpies $\Delta H_{df}(j)$ in GBCFO oxide are presented in Table 5.

**Table 5.** Defect formation enthalpies in GBCFO oxide as obtained from GGA + U calculations.

| Defect formation process | | $\Delta H_{df}(j)$, eV |
|---|---|---|
| $V_O$ formation | $FeO_6$ | 3.057 |
| | $FeO_5$ | 3.287 |
| | $FeO_4$ | 3.253 |
| $O_i$ formation | $FeO_5$ | 0.654 |
| | $FeO_4$ | 1.202 |

As can be seen, oxygen vacancies are very unlikely to form with the respective enthalpies computed to be higher than 3 eV. Still, these results align well with the experimental data[77] and can be explained by high energy penalties to convert $Fe^{3+}$ to $Fe^{2+}$ in perovskite-oxides. To add, the predicted trend of $FeO_6$ octahedra to be the sites which are most susceptible to hosting vacancies ($\Delta_{ox}$ parameter was found to be the lowest for $FeO_6$ polyhedra, see Table 4) seems to be supported by actual calculations, Table 5. On the other hand, the formation of interstitial oxygen appears to be intricated, although the relative fraction of $O_i$ defects (especially of those formed in $FeO_5$ layers) will be higher than that of oxygen vacancies in oxidative conditions (i.e. in air atmosphere). Still, as follows from the calculated results, the overall deviation of oxygen content in $GdBa_2Ca_2Fe_5O_{13\pm\delta}$ from 13 should be small ($|\delta|$ will be less than 0.01 at 1000 K and air atmosphere). The available thermogravimetric data support this conclusion – the measured mass change of GBCFO at heating in air was found to be negligible.[57] What is even more interesting is that the positive sign of $\Delta H_{df}$ of $O_i$ formation process implies that the fraction of interstitial oxygen will increase with temperature. Accordingly, the amount of holes in the VB will grow with heating. Given that $\Delta H_{df}(O_i) < \Delta H_{df}(V_O)$ and $\Delta H_{df}(O_i) > 0$, one can reasonably assume electron holes will be the main charge carriers in GBCFO at SOFC cathode conditions.

In agreement with the conclusions of the previous paragraph, the determination of $\langle\hat{\sigma}_{CRT}\rangle$ value was made assuming acceptor doping level ($p_d$) to be of $10^{17} – 10^{19}$ $cm^{-3}$ in magnitude, which roughly corresponds to $\delta \in [-10^{-5}, -10^{-3}]$ per $GdBa_2Ca_2Fe_5O_{13}$ formula unit. The estimated conductivity curves at $p_d < 10^{18}$ $cm^{-3}$ are shown in Figure 7(a) and reveal the transition from the extrinsic to the intrinsic regime as the temperature increases. One can acknowledge the obtained

$\langle\hat{\sigma}_{\mathrm{CRT}}\rangle$ numerical values at $p_d = 10^{17}$ cm$^{-3}$ are close to those ($\sigma_{exp}$) measured in experiment. Notably, when the doping amount is higher (i.e. $p_d = 10^{19}$ cm$^{-3}$), the shape of the conductivity plot becomes almost temperature independent. These results are nicely in agreement with the experimental findings. Indeed, defect formation enthalpies suggest that the concentration of holes should increase with temperature, i.e. $p_d = f(T)$. And hence, the experimentally observed $\sigma = f(T)$ of GBCFO originates from the intrinsic regime at low temperatures (due to the narrow band gap) and hole-doped regime, which is invoked by the incorporation of interstitial oxygen into the crystal lattice, at higher temperatures. Importantly, this mechanism qualitatively explains the flattening of $\sigma_{exp} = f(T)$ curve at T > 800 K, see Figure 7(a).

Accounting for the discussed crystalline anisotropy of GBCFO it is interesting to consider the direction-dependent components of $\hat{\sigma}_{\mathrm{CRT}}$. The respective data represented as $\sigma_{\mathrm{CRT}}/\tau$ functions are given in Figure 7(*b*). Those components of conductivity tensor that are parallel to either $[110]_p$ or $[-110]_p$ crystallographic directions (i.e. planes (001), also named planes *ab*) are 2 – 3 orders of magnitude higher than that parallel to the $[001]_p$ direction. To add, $\sigma_{\mathrm{CRT}}||[110]_p$ and $\sigma_{\mathrm{CRT}}||[-110]_p$ values are almost similar. Therefore, both magnitudes will be referred to as $\sigma_{\mathrm{CRT}}(||)$, while the quantity $\sigma_{\mathrm{CRT}}||[001]_p$ will be designated as $\sigma_{\mathrm{CRT}}(\perp)$. This denomination underlines that the obtained result shows direct evidence of the anisotropy of the GBCFO electrical properties. However, the reason behind the uncovered phenomenon seems to be unclear. In this sense, the previous computational study for the YBCFO suggested that the absence of oxygen ions in Y layer provided the main contribution to the 2D character of electronic conduction.[44] In turn, the present work provides a more complicated picture where all polyhedral layers in the GBCFO lattice play a certain role in providing the anisotropic behavior. As a result, the elimination of the $FeO_5$ square pyramids should provide more isotropic $\hat{\sigma}_{\mathrm{CRT}}$; the respective evaluations made for $GdBaCaFe_3O_8$ and presented as a ratio between $\sigma_{\mathrm{CRT}}(||)$ and $\sigma_{\mathrm{CRT}}(\perp)$ components of conductivity tensor clearly confirm this statement, see Fig. 8.

View Article Online
DOI: 10.1039/D5CP01780G



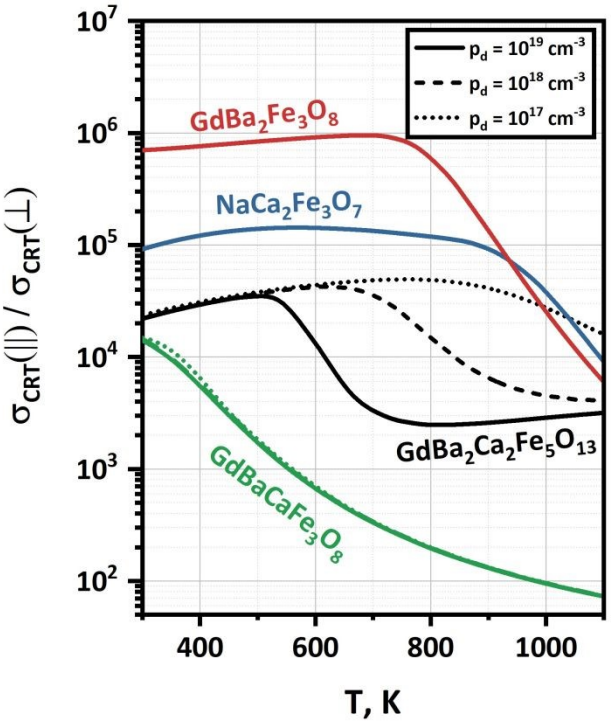


**Figure 8.** The ratio of $\sigma_{CRT}(||)$ to $\sigma_{CRT}(\perp)$ components of the conductivity tensor as a function of temperature and acceptor doping level calculated for different $Fe^{3+}$-containing oxides: $GdBa_2Ca_2Fe_5O_{13}$ (dark grey), $GdBa_2Fe_3O_8$ (red), $GdBaCaFe_3O_8$ (green) and $NaCa_2Fe_3O_7$ (dark blue).

In fact, the corresponding pDOS data suggest that the CB of $GdBaCaFe_3O_8$ is composed from electronic states of both $FeO_6$ and $FeO_4$ structural units (Fig. 4). Therefore, it can be deduced that in the case of GBCFO the main reason for the anisotropic behavior of $\hat{\sigma}_{CRT}$ is the combination of $FeO_5$ layers forming the bottom of CB and the large slabs composed of $FeO_6$ and $FeO_4$ polyhedra that provide effective isolation of the conduction slabs from each other. Because of that the curvature of the VB and CB along $[001]_p$ direction in GBCFO ($b_2$ direction in reciprocal space, as represented in Figure S6) is almost zero, resulting in effective mass for charge carriers and hence making $[001]_p$ direction highly unfavorable for electronic conduction in GBCFO. Similar behavior is observed for the $GdBa_2Fe_3O_8$ and $NaCa_2Fe_3O_7$ compounds (Figure 8).

## 4. Conclusions

DFT+U calculations on the $GdBa_2Ca_2Fe_5O_{13}$ perovskite-related oxide expose a distinct band structure that reveals a 2D-electronic behavior. The computing methodology (GGA+U approximation) used in this work captures both the nuclear and magnetic structures of the compound. The crystal structure, which consists of layered Gd/Ba/Ca ordering in combination with the ordering of three different coordination-polyhedron around the Fe-atoms ($FeO_6$-octahedra, $FeO_5$-squared pyramids and $FeO_4$-tetrahedra), causes a peculiar contribution of the

differently located Fe and O atoms to the resulting band structure. Both the valence and the conduction bands are shown to be spatially distributed in the lattice depending on the oxygen-coordination of the Fe atoms. In particular, the bottom of the CB is formed by 3d orbitals of Fe atoms possessing $3z^2 - r^2$ symmetry, that are located within the $FeO_5$-squared pyramids. However, the electronic states near the Fermi level are mainly formed by 2p states of oxygen atoms occupying the equatorial positions of the $FeO_6$-octahedra. As a result, $GdBa_2Ca_2Fe_5O_{13}$ appears to be a narrow-gap 2D-semiconductor (the respective band gap $E_g$ is found to be ~ 0.5 eV) where the $FeO_5$-layers create the CB, the $FeO_6$-layers form the VB and the $FeO_4$-layers create insulating channels avoiding the intralayer transport of electrons. The existence of the three types of oxygen-coordination around the Fe-atoms seems to be essential for the narrow band gap, since other possible double combinations of oxygen-polyhedra forming the anion sublattice, as well as singular ones lead to higher $E_g$ values. The computed pCOHP curves conclude a strongly bonding character of the chemical interaction between all the Fe atoms and the oxygens in the oxide and confirm the insulating character of the $FeO_4$ layers. Computed electronic conductivity tensors support the anisotropic electrical properties of the $GdBa_2Ca_2Fe_5O_{13}$, since the conductivity is established within the (ab)-planes (i.e. (001)p planes), but it is about three orders of magnitude lower along the c-axis ($[001]_p$ direction) of the structure. Overall, the band-structure of the $GdBa_2Ca_2Fe_5O_{13}$ oxide is consequence of the existence and ordering of the three different types of $FeO_x$ polyhedra within the crystal structure.

**Acknowledgements**

This research has been supported by the "Plan de Recuperación, Transformación y Resiliencia-C17.I1", with funds from the European Union - Next Generation EU, "European Regional Development Fund" as part of the action after the COVID-19 pandemic, and Comunidad de Madrid for the project "(GREEN H2-CM). Authors also thank MCIN/AEI/10.13039/501100011033 for funding the Project PID2022-139039OB-C22 and MCIN/AEI/10.13039/501100011033/"NextGenerationEU"/PRTR for funding the Project TED2021-130452B-C21. Special thanks to Mikhail Kalinkin from the Institute of Solid State Chemistry UB RAS for measuring optical spectra.

**Supporting information**

The structural and magnetic data of various oxides used in the DFT + U calculations (Table S1); Graphic representations of $GdBaCaFe_3O_8$, $GdBa_2Fe_3O_8$ and $NaCa_2Fe_3O_7$ crystal structures (Figure S1); Graphic representations of disordered $GdBa_2Ca_2Fe_5O_{13}$ crystal structures (Figure S2);

The computed energy-volume curve for the $GdBa_2Ca_2Fe_5O_{13}$ oxide and the respectively derived Debye temperature and unit cell volume dependences on temperature (Figure S3); The optimized coordinates of the G-AFM $GdBa_2Ca_2Fe_5O_{13}$ unit cell (Table S2); The comparison of GGA + U computed densities of states for $GdFeO_3$ ferrites with and without accounting for the 4f states of Gd atoms (Figure S4); The GGA + U computed optical spectra for the G-AFM $GdBa_2Ca_2Fe_5O_{13}$ oxide (Figure S5); Computed band dispersions of orthorhombic $GdBa_2Ca_2Fe_5O_{13}$ unit cell with G-AFM magnetic ordering (Figure S6); Charge density projections of CB and VB of the G-AFM $GdBa_2Ca_2Fe_5O_{13}$ along $[100]_p$ direction (Figure S7); The GGA + U computed band dispersion and experimentally measured optical absorption spectrum of $CaBaFe_4O_8$ oxide (Figure S8); The DOS/pDOS spectra of $GdFeO_3$, $BaCaFe_2O_5$ and $CaBaFe_4O_8$ as obtained within the GGA + U framework (Figure S9).

## References

**1.** T. Ishihara, in *Springer Handbook of Electronic and Photonic Materials*, eds. S. Kasap, P. Capper, Springer Cham, 2017, Inorganic Perovskite Oxides.

**2.** T. Wolfram, S. Ellialtioglu, *Electronic and optical properties of d-band perovskites*, Cambridge University Press, Cambridge, 2006.

**3.** D. I. Khomskii, *Transition metal compounds*, Cambridge University Press, Cambridge, 2014.

**4.** M. Nasir, I. Kim, K. Lee, S.I. Kim, K. H. Lee, H.J. Park. *Physical Chemistry Chemical Physics*, 2023, **25(5)**, 3942-3949.

**5.** J. Ding, X. Zhu. *Journal of Materials Chemistry C*, 2024, **12,** 9510-9561.

**6.** J. Irvine, J. L. Rupp, G. Liu, X. Xu, S. Haile, X. Qian, et al. *Journal of Physics: Energy*, 2021, **3(3)**, 031502.

**7.** G. R. Monama, K. E. Ramohlola, E. I. Iwuoha, K. D. Modibane. *Results in Chemistry*, 2022, **4**, 100321.

**8.** X. Liang, W. Yan, Y. Yu, K. Zhang, W. An, H. Chen et al. *Angewandte Chemie International Edition*, 2023, **62(46)**, e202311606.

**9.** A. N. Zainon, M. R. Somalu, A. M. K. Bahrain, A. Muchtar, N. A. Baharuddin, M. A. et al. *International Journal of Hydrogen Energy*, 2023, **48**(53), 20441-20464.

**10.** S. E. Wolf, F. E. Winterhalder, V. Vibhu, L. B. de Haart, O. Guillon, R. A. Eichel, & N. H. Menzler. *Journal of Materials Chemistry A*, 2023, **11**(34), 17977-18028.

**11.** W. Zhang & Y. H. Hu. *Catalysis Today*, 2023, **409**, 71-86.

**12.** S. Baratov, E. Filonova, A. Ivanova, M. B. Hanif, M. Irshad, M. Z. Khan et al. *Journal of Energy Chemistry*, 2024, **94**, 302-331.

View Article Online
DOI: 10.1039/D5CP01780G

**13.** E. Tezel, D. Guo, A. Whitten, G. Yarema, M. Freire, R. Denecke et al. *Journal of The Electrochemical Society*, 2022, **169**(3), 034532.

**14.** A. I. Klyndyuk, E. A. Chizhova, D. S. Kharytonau, D. A. Medvedev. *Materials*, 2022, **15**, 141.

**15.** J. A. Kilner & M. Burriel. *Annual Review of Materials Research*, 2014, **44**(1), 365-393.

**16.** J. H. Kim & A. Manthiram. *Journal of Materials Chemistry A*, 2015, **3**(48), 24195-24210.

**17.** F. Fauth, E. Suard, V. Caignaert, B. Domenges, I. Mirebeau, L. Keller. *The European Physical Journal B-Condensed Matter and Complex Systems*, 2001, **21**, 163-174.

**18.** Z. Gao, L. V. Mogni, E. C. Miller, J. G. Railsback, S. A. Barnett. *Energy & Environmental Science*, 2016, **9**(5), 1602-1644.

**19.** P. Winiarz, E. A. Sroczyk, A. Brzoza-Kos, P. Czaja, K. Kapusta, K. Świerczek. *Acta Materialia*, 2024, **277**, 120186.

**20.** A. A. Taskin, A. N. Lavrov, & Y. Ando. *Progress in Solid State Chemistry*, 2007, **35**(2-4), 481-490.

**21.** D. Parfitt, A. Chroneos, A. Tarancón, J. A. Kilner. *Journal of Materials Chemistry*, 2011, **21**(7), 2183-2186.

**22.** R. Pelosato, G. Cordaro, D. Stucchi, C. Cristiani, G. Dotelli. *Journal of Power Sources*, 2015, **298**, 46-67.

**23.** D. Muñoz-Gil, D. Pérez-Coll, E. Urones-Garrote, U. Amador, S. García-Martín. *Journal of Materials Chemistry A*, 2017, **5**(24), 12550-12556.

**24.** D. Muñoz-Gil, E. Urones-Garrote, D. Pérez-Coll, U. Amador, S. García-Martín. *Journal of Materials Chemistry A*, 2018, **6**(13), 5452-5460.

**25.** D. Muñoz-Gil, D. Ávila-Brande, E. Urones-Garrote, S. García-Martín. *Dalton Transactions*, 2015, **44**(23), 10867-10874.

**26.** S. García-Martín, K. Manabe, E. Urones-Garrote, D. Ávila-Brande, N. Ichikawa, Y. Shimakawa. *Inorganic Chemistry*, 2017, **56**(3), 1412-1417.

**27.** P. Karen. *Journal of Solid State Chemistry*, 2021, **299**, 122147.

**28.** P. Karen, E. Suard, F. Fauth. *Inorganic Chemistry*, 2005, **44**(23), 8170-8172.

**29.** J. M. Hudspeth, D. J. Goossens, A. J. Studer, R. L. Withers, L. Norén. *Journal of Physics: Condensed Matter*, 2009, **21**(12), 124206.

**30.** R. Marín-Gamero, X. Martinez de Irujo-Labalde, E. Urones-Garrote, S. García-Martín. *Inorganic Chemistry*, 2020, **59**(8), 5529-5537.

**31.** X. M. de Irujo-Labalde, U. Amador, C. Ritter, M. Goto, M. A. Patino, Y. Shimakawa, S. García-Martín. *Inorganic Chemistry*, 2021, **60**(11), 8027-8034.

**32.** G. Kresse & J. Furthmüller. *Computational Materials Physics, Faculty of Physics. Universitat Wien*, 2014.

**33.** J. Sun, A. Ruzsinszky, J. P. Perdew. *Physical Review Letters*, 2015, **115**(3), 036402.

**34.** H. D. Saßnick, C. Cocchi. *Electronic Structure*, 2021, **3**(2), 027001.

**35.** J. He, C. Franchini. *Physical Review B—Condensed Matter and Materials Physics*, 2012, **86**(23), 235117.

**36.** S. L. Dudarev, G. A. Botton, S. Y. Savrasov, C. J. Humphreys, A. P. Sutton. *Physical Review B*, 1998, **57**(3), 1505.

**37.** J. K. Shenton, D. R. Bowler, W. L. Cheah. *Journal of Physics: Condensed Matter*, 2017, **29**(44), 445501.

**38.** L. Wang, T. Maxisch, G. Ceder. *Physical Review B—Condensed Matter and Materials Physics*, 2006, **73**(19), 195107.

**39.** M. Alaydrus, I. Hamada, Y. Morikawa. *Physical Chemistry Chemical Physics*, 2021, **23**(34), 18628-18639.

**40.** M. Gómez-Toledo, S. A. López-Paz, S. García-Martín, M. E. Arroyo-de Dompablo. *Inorganic Chemistry*, 2023, **62**(8), 3445-3456.

**41.** M. Ferri, J. Elliott, S. Fabris, S. Piccinin. *Physical Review B*, 2020, **101**(15), 155201.

**42.** B.-L. Liu, Y.-C. Wang, Y. Liu, Y.-J. Xu, X. Chen, H.-Z. Song, Y. Bi, H.-F. Liu, H.-F. Song. *Journal of Chemical Physics*, 2023, **158**, 084108.

**43.** A. Otero-De-La-Roza, D. Abbasi-Pérez, V. Luaña, *Computer Physics Communications*, 2011, **182**(10), 2232-2248.

**44.** X. M. de Irujo-Labalde, M. Goto, E. Urones-Garrote, U. Amador, C. Ritter, M. Amano-Patino et al. *Chemistry of Materials*, 2024, **36**(10), 5184-5191.

**45.** A. Demont, M. S. Dyer, R. Sayers, M. F. Thomas, M. Tsiamtsouri, H. N. Niu et al. *Chemistry of Materials*, 2010, **22**(24), 6598-6615.

**46.** C. Tenailleau, M. Allix, J. B. Claridge, M. Hervieu, M. F. Thorpe, R. J. Cava. *Journal of Solid State Chemistry*, 2003, **176**(2), 381-392.

**47.** X. M. de Irujo-Labalde, E. Urones-Garrote, S. García-Martín. *Solid State Sciences*, 2024, **151**, 107516.

**48.** O. A. Salawu, S. Boulfrad, U. Schwingenschlögl, *J. Mater. Chem. A*, 2016, **4**(9), 3560-3564.

**49.** M. F. Hoedl, C. Ertural, R. Merkle, R. Dronskowski, J. Maier. *The Journal of Physical Chemistry C*, 2022, **126**(30), 12809-12819.

**50.** M. Gajdoš, K. Hummer, G. Kresse, J. Furthmüller, F. Bechstedt. *Physical Review B—Condensed Matter and Materials Physics*, 2006, **73**(4), 045112.

**51.** V. Wang, N. Xu, J. C. Liu, G. Tang, W. T. Geng. *Computer Physics Communications*, 2021, **267**, 108033.

**52.** R. Dronskowski, P. E. Blöchl. *Journal of Physical Chemistry*, 1993, **97**, 8617-8624.



View Article Online
DOI: 10.1039/D5CP01780G

**53.** G. K. Madsen, J. Carrete, M. J. Verstraete. *Computer Physics Communications*, 2018, **231**, 140-145.

**54.** P. E. Blöchl, O. Jepsen, O. K. Andersen. *Physical Review B*, 1994, **49**(23), 16223.

**55.** H. Weihe, H. U. Güdel. *Inorganic Chemistry*, 1997, **36**(17), 3632-3639.

**56.** T. Katsura, Y. Tange. *Minerals*, 2019, **9**(12), 745.

**57.** Marín Gamero, R. (2024). Óxidos metálicos con superestructura derivada de la perovskita y estudio de sus propiedades electrocatalíticas en la reducción de oxígeno.

**58.** A. Scrimshire, A. Lobera, A. M. T. Bell, A. H. Jones, I. Sterianou, S. D. Forder, P. A. Bingham, *Journal of Physics: Condensed Matter*, 2018, **30**(10), 105704.

**59.** S. Lutfalla, V. Shapovalov, A. T. Bell. *Journal of Chemical Theory and Computation*, 2011, **7**(7), 2218-2223.

**60.** P. Adler, U. Schwarz, K. Syassen, A. P. Milner, M. P. Pasternak, M. Hanfland. *Journal of Solid State Chemistry*, 2000, **155**(2), 381-388.

**61.** M. Capone, C. J. Ridley, N. P. Funnell, M. Guthrie, C. L. Bull. *Physica Status Solidi (b)*, 2021, **258**(2), 2000413.

**62.** E. Marelli, J. Lyu, M. Morin, M. Leménager, T. Shang, N. S. Yüzbasi et al. *EES Catalysis*, 2024, **2**(1), 335-350.

**63.** U. Von Barth, C. D. Gelatt. *Physical Review B*, 1980, **21**(6), 2222.

**64.** X. H. Zhu, X. B. Xiao, X. R. Chen, & B. G. Liu. *RSC Advances*, 2017, **7**(7), 4054-4061.

**65.** V. R. Galakhov, E. Z. Kurmaev, K. Kuepper, M. Neumann, J. A. McLeod, A. Moewes et al. *The Journal of Physical Chemistry C*, 2010, **114**(11), 5154-5159.

**66.** X. Bo, D. Wang, X. G. Wan. *Physics Letters A*, 2021, **394**, 127202.

**67.** B. Ouyang, T. Chakraborty, N. H. Perry, T. Mueller, N. R. Aluru, E. Ertekin. *Chemistry of Materials*, 2019, **31**(9), 3144-3153.

**68.** M. D. Scafetta, A. M. Cordi, J. M. Rondinelli, S. J. May. *Journal of Physics: Condensed Matter*, 2014, **26**(50), 505502.

**69.** M. K. Warshi, V. Mishra, A. Sagdeo, V. Mishra, R. Kumar, P. R. Sagdeo. *Ceramics International*, 2018, **44**(7), 8344-8349.

**70.** Encyclopedia Britannica, https://www.britannica.com/science/color, (accessed April 2025).

**71.** J. Schanda (Ed.). *Colorimetry: Understanding the CIE System*, John Wiley & Sons, 2007.

**72.** Y. Shin, K. Y. Doh, S. H. Kim, J. H. Lee, H. Bae, S. J. Song, D. Lee. *Journal of Materials Chemistry A*, 2020, **8**(9), 4784-4789.

**73.** A. D. Bamburov, A. A. Markov, M. V. Patrakeev, I. A. Leonidov. *Solid State Ionics*, 2019, **332**, 86-92.

**74.** J. E. Auckett, G. J. McIntyre, M. Avdeev, H. De Bruyn, T. T. Tan, S. Li, C. D. Ling. *Journal of Applied Crystallography*, 2015, **48**(1), 273-279.
View Article Online
DOI: 10.1039/D5CP01780G
**75.** I. Kim, H. Lee, M. Choi. *Journal of Applied Physics*, 2022, **131**(7), 075106.

**76.** V. P. Zhukov, E. V. Chulkov. *Physics of the Solid State*, 2022, **64**(4), 422-431.

**77.** I. A. Leonidov, A. A. Markov, M. A. Zavyalov, O. V. Merkulov, E. V. Shalaeva, S. S. Nikitin et al. *Materials*, 2022, **15**(13), 4390.

The data supporting this article have been included as part of the Supplementary Information View Article Online
DOI: 10.1039/D5CP01780G

Yours sincerely,

Prof. SGM and Dr. BVP